iJRASET
International Journal For Research in Applied Science and Engineering Technology

INTERNATIONAL JOURNAL FOR RESEARCH

IN APPLIED SCIENCE & ENGINEERING TECHNOLOGY

Volume: 13 **Issue:** VII **Month of publication:** July 2025

DOI: https://doi.org/10.22214/ijraset.2025.73229

www.ijraset.com

Call: 08813907089 | E-mail ID: ijraset@gmail.com

International Journal for Research in Applied Science & Engineering Technology (IJRASET)
ISSN: 2321-9653; IC Value: 45.98; SJ Impact Factor: 7.538
Volume 13 Issue VII July 2025- Available at www.ijraset.com

Heat and Mass Transfer Effect of Micropolar Nanofluid Flow over a Horizontal Moving Plate with Non-Uniform Heat Source/Sink

Machindranath Diwate[1], Jagadish V. Tawade[2], Pradeep G Janthe[3], Nitiraj V. Kulkarni[4]
[1]*Department of Mathematics, Sinhgad Institute of Technology and Science, Narhe Pune-411041, India*
[3]*Sinhgad Academy of Engineering, Kondhwa(Bk) Pune – 411048, India*
[1,2,4]*Department of Mathematics, Vishwakarma University, Pune-411048, India*

Abstract: ***This study investigates the stagnation-point flow and heat transfer in mixed convection of a micropolar fluid over an exponentially expanding vertical sheet, including the effects of buoyancy, magnetic fields, radiation, and viscous dissipation. The governing partial differential equations (PDEs) are transformed into ordinary differential equations (ODEs) using similarity transformations and solved with the bvp4c method. The results show that increasing buoyancy, magnetic field, radiation, and viscous dissipation enhance the velocity profile near the surface. Buoyancy suppresses particle rotation, while magnetic fields enhance it, with micropolar fluids reversing this trend under higher radiation. Temperature decreases with stronger magnetic fields and buoyancy, indicating improved heat dissipation. Differences in fluid behaviour between micropolar and Newtonian fluids highlight the unique characteristics of micropolarity. These findings are relevant for applications such as polymer extrusion, thin-film manufacturing, microfluidic devices, lubrication systems, and cooling technologies, where precise control of flow and heat transfer is essential.***

Keywords: ***Micropolar fluid, Exponential stretching/shrinking sheet, Magnetohydrodynamics, Viscous dissipation, Stagnation point flow.***

I. INTRODUCTION

In recent years research on flow of the boundary layer based on fluids that are non-Newtonian and Newtonian have numerous applications for fluids on stretching surfaces in engineering and industry, such as hot rolling and manufacturing of plastic film, artificial fibres, wire drawing, copper wire annealing and tinning, Production of glass fibre, paper, and plastic sheets made from polymers, and polymeric sheets made from extruded materials and heat-treated materials that passing on conveyor belts or between feed and wind-up rollers.

Sakiadis [1,2] first investigated boundary-layer flow on continuous solid surfaces, establishing the foundational framework for fluid dynamics over moving sheets. Crane [3] extended this by analyzing fluid flow over stretching plates, while Gupta and Gupta [4] studied the effects of suction and blowing on heat and mass transfer over stretched surfaces. Sandeep and Sulochana [5] explored dual solutions for unsteady MHD micropolar fluid flows over stretching/shrinking sheets with non-uniform heat sources, emphasizing the influence of unstable conditions. Prasannakumara et al. [6] examined the melting phenomenon in dusty fluid flows near stagnation points, accounting for the role of thermal radiation. Mabood et al. [7] analyzed the Soret effect and non-uniform heat sources in hydromagnetic micropolar fluids, providing insights into non-Darcian flows. Seth et al. [8] studied MHD stagnation-point flow over exponentially stretching sheets, incorporating free-stream motion and viscous dissipation. Ram et al. [9] advanced this research through the numerical simulation of micropolar fluid flows with activation energy and bilateral reactions, improving the predictive modeling of complex systems. Murugan et al. [10-12] conducted comprehensive research on hybrid nanofluid flows. They examined mixed convection over rotating cones with interfacial nanolayer effects [10], entropy generation in MHD hybrid nanofluids within porous media under thermo-radiation [11], and energy transfer in Maxwell thin-film fluid flows [12], illustrating the interaction between heat transfer and fluid motion in advanced engineering systems.

Tarakaramu et al. [13,14] focused on 3D MHD nanofluid flows, studying Arrhenius activation energy with convective boundary conditions [13] and analyzing thermal radiation and heat generation in Casson fluid flows over porous stretching surfaces [14]. Masthanaiah et al. [15] explored viscous dissipation and entropy generation in cold liquid flows through porous channels, providing key insights for optimizing industrial cooling systems. Jagadeesh et al. [16] investigated heat and mass transfer in 3D Williamson nanofluid flows along stretching sheets, demonstrating that thermal radiation and absorption enhance heat transfer.

Reddy and Kumar [17] tackled cloud computing security and efficiency using DROPS and T-coloring methods, showcasing improvements in data integrity and resource utilization. Li et al. [18] explored heat transfer in 3D nanofluid flows, highlighting how anisotropic slip and magnetic fields improve thermal management systems. Sedki and Qahiti [19] investigated chemically reactive Casson nanofluid flow over stretchable surfaces, revealing the influence of variable surface thickness on fluid behaviour. Rehman et al. [20] analyzed MHD stagnation-point flow of nanofluids over exponentially stretching sheets, emphasizing the impact of thermophysical properties on heat transfer efficiency.

Bejawada and Nandeppanavar [21] studied MHD micropolar fluid flows over vertical porous plates, showing that thermal radiation enhances heat transfer and stabilizes the boundary layer. Bakar and Soid [22] examined MHD stagnation-point flows in micropolar fluids over exponentially vertical sheets, identifying the impact of sheet expansion on heat transfer dynamics. Khan et al. [23-27] conducted extensive studies on hybrid nanofluids, including bioconvective Casson hybrid nanofluids [23], solar thermal heat exchangers [24], chemically reactive micropolar Williamson hybrid nanofluids [25], Maxwell fluid flows with mixed convection [26], and tangent hyperbolic nanofluid flows over porous cylinders [27], demonstrating the practical applications of hybrid materials in advanced thermal systems. Waini et al. [28] examined hybrid nanofluid flow towards a stagnation point over an exponentially stretching/shrinking vertical sheet, accounting for buoyancy effects and revealing improved heat transfer behaviour. Bakar and Soid [29] further analyzed MHD stagnation-point flow and heat transfer in micropolar fluids over exponentially vertical sheets, demonstrating the significant influence of buoyancy and sheet expansion on fluid behaviour. Yasir et al. [30-33] contributed valuable insights into various interdisciplinary applications of fluid dynamics, analyzing thermophoretic particle deposition with Soret-Dufour effects [30], mathematical modeling of MEMS systems [31], nanoscale energy transport in micropolar fluids [32], and the impact of Arrhenius activation energy on viscous micropolar fluid flows with gyrotactic microorganisms [33].

In real-world applications, exponentially expanding surfaces are frequently encountered in advanced manufacturing and thermal processing industries. The rapid expansion of a vertical sheet provides unique benefits. For instance, in polymer extrusion processes, such behaviour enhances cooling efficiency by increasing surface area and convective heat transfer rate. Similarly, in thin-film manufacturing, an expanding surface improves the uniformity of material deposition.

In the context of micropolar fluid dynamics and magnetohydrodynamics (MHD), the fast expansion of the sheet generates complex boundary layer behaviour, where the interplay of fluid microstructure and external magnetic fields becomes more pronounced. The exponentially increasing sheet velocity enables researchers to observe the influence of parameters such as magnetic forces, viscous dissipation, and buoyancy in non-linear regimes, thus offering deeper insight into mixed convection phenomena.

The novelty behind this study lies in the growing importance of understanding complex fluid dynamics, particularly in micropolar fluids, which exhibit unique micro-rotational effects not seen in classical Newtonian fluids. Micropolar fluids have significant applications in advanced engineering processes, such as polymer extrusion, thin-film manufacturing, and microfluidics, where precise control of flow and heat transfer is critical. Additionally, the behaviour of such fluids under the influence of magnetic fields, buoyancy forces, and radiation remains an area of active research due to its relevance to cooling technologies and environmental applications.

II. METHODOLOGY

Imagine a scenario where a micropolar fluid moves along a upright surface toward a point of stagnation, The x and y axes in Figure (4.1) are Cartesian coordinates allocated horizontal and vertically within the surface, whereas y axis is perpendicular to x axis, with the origin O. $u_e(x) = ae^{x/L}$, $a > 0$ is free stream velocity and L is reference length. Next, exponential velocity is $u_w(x) = be^{x/L}$ as $b > 0$ surface is stretched, $b < 0$ shrunk, $b = 0$ for static surface. $T_w(x) = T_\infty + T_0 e^{2x/L}$ is surface temperature where T_0, T_∞ is constant and ambient temperature respectively. Hence, g is acceleration.

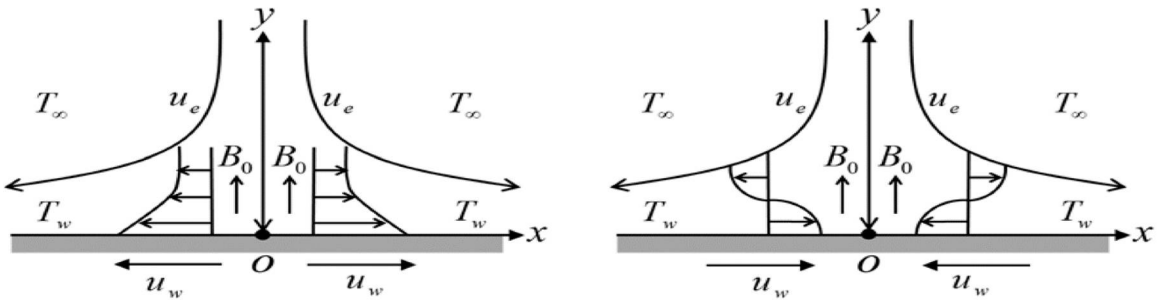

Fig. 1 The flow configuration for (a) a stretching sheet and (b) a shrinking sheet.

Partial differential equations (PDEs) for continuity, linear momentum, rotational momentum, and energy are the forms that regulate the boundary layer parabolic partial differential equations (PDEs).

$$\frac{\partial u}{\partial x}+\frac{\partial v}{\partial y}=0 \tag{1}$$

$$u\frac{\partial u}{\partial x}+v\frac{\partial v}{\partial y}=u_e\frac{\partial u_e}{\partial x}+\left(\nu+\frac{K}{\rho}\right)\frac{\partial^2 u}{\partial y^2}+\frac{K}{\rho}\frac{\partial N}{\partial y}+g\beta_T(T-T_\infty)-\frac{\sigma}{\rho}B^2(u-u_e) \tag{2}$$

$$u\frac{\partial N}{\partial x}+v\frac{\partial N}{\partial y}=\frac{\chi}{\rho j}\frac{\partial^2 N}{\partial y^2}-\frac{k}{\rho j}\left(2N+\frac{\partial u}{\partial y}\right) \tag{3}$$

$$u\frac{\partial T}{\partial x}+v\frac{\partial T}{\partial y}=\frac{k}{\rho c_p}\frac{\partial^2 T}{\partial y^2}-\frac{1}{\rho c_p}\frac{\partial q_r}{\partial y}+\frac{\mu}{\rho c_p}\left(\frac{\partial u}{\partial y}\right)^2+\frac{\sigma B^2u^2}{(\rho c)_p}+\frac{q'''}{(\rho c)_p} \tag{4}$$

In accordance with the imposed boundary constraints:

$$\left.\begin{gathered}u=u_w,\quad v=0,\quad T=T_w,\quad N=-m\frac{\partial u}{\partial y}\ at\ y=0.\\ u\to u_e,\quad T\to T_\infty,\quad N\to 0\ as\ y\to\infty\end{gathered}\right\} \tag{5}$$

The fluid density is symbolized by ρ, the microrotation/angular velocity is denoted by N, the micro-inertia per unit mass is $j=2Lve^{-x/L}/a$, Spin gradient is $\chi=\mu(1+K/2)j$, k represent vortex viscosity. σ represent electrical conductivity of fluid, $B(X)=B_0e^{x/2L}$ denotes variable magnetic field where B_0 a constant is and specific heat is denoted by c_p and β_T is symbol of coefficient thermal expansion, the kinematic viscosity is $\nu=\mu/\rho$, μ represents the fluid viscosity coefficient. Equation (1) to Equation (4) under the boundary condition Equation (5) can be simplified using following similarity transformation Waini et al., [28] and Bakar et al., [29]:

$$\left.\begin{gathered}\eta=\sqrt{\frac{a}{2\nu L}}e^{x/2L}y,\quad u=ae^{x/L}f'(\eta),\quad v=-\sqrt{\frac{a\nu}{2L}}e^{\frac{x}{2L}}\left(f(\eta)+\eta f'(\eta)\right),\\ \theta(\eta)=\frac{T-T_\infty}{T_w-T_\infty},\quad N=a\sqrt{\frac{a}{2\nu L}}e^{3x/2L}h(\eta)\end{gathered}\right\} \tag{6}$$

Where similarity variable is η, a stream function that fulfils equation (1) identically is indicated by the symbols u and v. Hence, the converted equations linear momentum (2), angular momentum (3) and energy (4) become:

$$f'''(1+K)+f''f-2(f')^2-M(f'-1)+Kh'+2\lambda\theta+2=0 \tag{7}$$

$$\left(1+\frac{K}{2}\right)h''-K(2h+f'')-3f'h+fh'=0 \tag{8}$$

$$Pr\,(4f'\theta-f\theta')-\theta''\left(1+\frac{4R}{3}\right)-Pr\,Ec((f'')^2+M(f')^2)+(A^*f'+B^*\theta)=0 \tag{9}$$

The corresponding boundary conditions [See Ref. 33]:

$$\left.\begin{gathered}f(\eta)=0,\quad f'(\eta)=\varepsilon,\quad \theta(\eta)=1,\quad \mathrm{h}(\eta)=-mf''(\eta)\ at\ \eta=0.\\ f'(\eta)\to 1,\quad \theta(\eta)\to 0,\quad h(\eta)\to 0\ as\ \eta\to\infty\end{gathered}\right\} \tag{10}$$

Prime indicates derivative w.r.t η and $M=2\sigma B_0^2L/\rho a$ denotes Magnetic parameter. Buoyancy parameter is $\lambda=g\beta_TT_0L/a^2$, the stretching/shrinking parameter is $\varepsilon=\frac{b}{a}$, $a>0$. For $(b>0)$ surface undergoes stretching and for $(b<0)$ the surface is shrunk. Thus, there exists a direct proportionality between ε and b. Next, $Pr=\frac{\mu c_p}{k}$, $K=k/\mu$ and $R=4\sigma^*T_\infty^3/k^*$ are Prandtl number, micropolar and radiation parameter respectively. The associated physical parameters encompass the local Nusselt number Nu_x, the local couple stress M_x, the skin friction coefficient C_f.

$$C_f=\frac{\tau_w}{\rho u_e^2},\qquad M_x=\frac{\chi\left(\frac{\partial N}{\partial y}\right)_{y=0}}{\rho x u_e^2},\qquad Nu_x=-\frac{x}{(T_w-T_\infty)}\left(\frac{\partial T}{\partial y}\right)_{y=0} \tag{11}$$

Where the surface shear stress is:

$$\tau_w=\left[(\mu+k)\frac{\partial u}{\partial y}+kN\right]_{y=0}$$

Then, local Nusselt number, reduced skin friction and local couple stress:

$$\left.\begin{aligned} Nu_x(Re_x)^{1/2}\sqrt{\frac{2L}{x}} = -\theta'(0), \qquad C_f(Re_x)^{1/2}\sqrt{\frac{2L}{x}} = [1+(1-m)K]f''(0), \\ M_x Re_x = \left(1+\frac{K}{2}\right)h'(0) \end{aligned}\right\} \tag{12}$$

The local Reynolds number is represented by $Re_x = xu_e/\nu$

III.NUMERICAL SOLUTION

To change the structure of partial differential equations (PDEs) into a more manageable form Similarity transformations are employed. thereby transforming the original problem in a structure of ordinary differential equations (ODEs). This reduction streamlines analysis by transforming the equations into a one-dimensional form, thereby facilitating the numerical computation of velocity, microrotation, and temperature distributions.

Using MATLAB's *bvp4c* solver the boundary value problem is solved, which is well-suited for handling differential equations defined with boundary conditions at surface $(\eta = 0)$ and at a faraway from surface $(\eta \to \infty)$. The solver adapts the mesh based on solution behaviour to ensure accuracy and convergence, particularly in regions with steep gradients near the surface.

This numerical solution allows detailed exploration of the outcomes of key physical factors for example micropolar effects, magnetic field intensity, buoyancy forces, thermal radiation, and viscous dissipation influence the fluid's dynamic motion as well as its heat transfer characteristics. The results offer insights into flow control and heat management, relevant for processes like polymer extrusion, thin-film manufacturing, and microfluidic devices.

Equations (7)-(9) are solved as follows;

$$f = f_1, f' = f_2, f'' = f_3, \tag{13}$$

$$h = f_4, h' = f_5, \tag{14}$$

$$\theta = f_6, \theta' = f_7, \tag{15}$$

$$f''' = \left(\frac{1}{(1+K)}\right)[M(f_2-1) - f_3 f_1 + 2(f_2)^2 - Kf_5 - 2\lambda f_6 - 2] \tag{16}$$

$$h'' = \left(\frac{1}{\left(1+\frac{K}{2}\right)}\right)(K(2f_4+f_3) + 3f_2 f_4 - f_1 f_5) \tag{17}$$

$$\theta'' = \frac{1}{\left(1+\frac{4R}{3}\right)}[Pr\,(4f_2 f_6 - f_1 f_7) - Pr\,Ec(f_3^2 + Mf_2^2) + (A^* f_2 + B^* f_6)] \tag{18}$$

Corresponding boundary conditions are expressed as, (19)

$$\left.\begin{aligned} f_1(0) = 0, \quad f_2(0) = \varepsilon, \quad f_6(0) = 1, \quad f_4(0) = -mf_3(0) \\ f_2(1) = 1, \quad f_6(1) = 0, \quad f_4(1) = 0 \end{aligned}\right\}$$

By suitably assuming the missing slopes f' and $\theta\ at\ \eta = 0$, for ease of numerical computation, which is then solved through the application of the appropriate shooting technique for the set of the parameters that appear in governing equations and have acknowledged the values for f' and $\theta\ at\ \eta = 0$. The shooting technique's initial circumstances must be estimated rather accurately for the convergence criterion to work. After the difference between most recent iterative value of f' and prior iterative value of f' is equal, the iterative process is terminated. Once convergence is attained, the needed solution is obtained by integrating the resulting ODE with the usual *bvp4c* method with a supplied set of parameters.

To investigate, the flow model from the aforementioned coupled ODEs (16)-(18) for different values of regulating parameters like $Ec, M, S,\ and\ Pr,$ an efficient *bvp4c* method was used. The coupled ODEs (16)-(18) are in 3rd, 2nd, and 2nd order respectively which are reduced in the form of simultaneous equations for 5 unknowns.

The comparison of numerical data in Tables I and II revealed excellent consistency between the current outcomes and earlier research, thereby validating the accurateness and efficiency of the applied technique. As the stretching/shrinking parameter rises, the skin friction coefficient decreases, while an conflicting trend is detected for the local Nusselt number, which rises accordingly.

Table I

Comparison for Numerical Values $C_f(Re_x)^{1/2}\sqrt{2L/x}$ for $\varepsilon = -0.5, 0, 0.5$

ε	Ur Rehman *et al.*, [20]	Waini *et al.*, [28]	Bakar & Soid[29]	Present Study
-0.5		2.1182	2.11816867	2.11816850
0	1.68720	1.6872	1.68721817	1.68721800
0.5	0.96040	0.9604	0.96041608	0.96041604

Table II

Comparison for Numerical Values $Nu_x(Re_x)^{1/2}\sqrt{2L/x}$ for $\varepsilon = -0.5, 0, 0.5$

ε	Waini et al., [28]	Bakar & Soid [29]	Present Study
-0.5	0.0588	0.05878644	0.05878630
0	2.5066	2.50662545	2.50662532
0.5	4.8016	4.08157327	4.08157320

Parameters of micropolar K, buoyancy λ, magnetic M and radiation R will be examined. The other factors for example the material parameter m and Prandtl number Pr are set to $m = 0.5$ and $Pr = 6.2$ are considered.

IV. RESULT AND DISCUSSION

In this section, we present the analysis of micropolar fluid flow and heat transfer over an exponentially stretching/shrinking vertical surface, supported by numerical simulations. The results are discussed for velocity, angular velocity, temperature, and heat transfer characteristics. Various governing parameters, such as the magnetic field parameter M, micropolar parameter K, radiation parameter R, buoyancy parameter λ, Eckert number Ec, and Prandtl number Pr, are varied to study their effects. The numerical solutions for velocity $f'(\eta)$, angular velocity $h(\eta)$, and temperature $\theta(\eta)$ profiles are presented and analyzed with appropriate physical interpretations.

For each case, asymptotic behaviour is ensured by satisfying the boundary conditions, and the numerical results validate the consistency of the solutions. The figures corresponding to different parameter values provide detailed insights into the flow structure and temperature field.

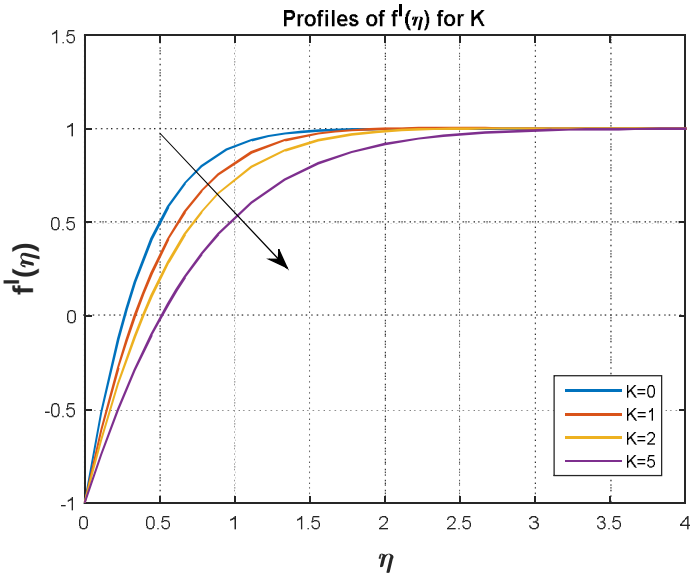

Fig. 2 Profiles of $f'(\eta)$ for K

Fig. 2 illustrates the velocity profiles $f'(\eta)$ for various values of the micropolar parameter K. As K increases from 0 to 5, the velocity near the surface decreases due to enhanced rotational inertia introduced by the fluid's microstructure, which resists the flow.

For $K = 0$, representing a Newtonian fluid, the velocity is highest, whereas higher K values reflect greater micropolarity, slowing down the flow. Regardless of the value of K, all profiles converge asymptotically to $f'(\eta) \to 1$ as $\eta \to \infty$, indicating that the fluid eventually attains the free-stream velocity. This demonstrates that increasing micropolarity delays the transition in the boundary layer.

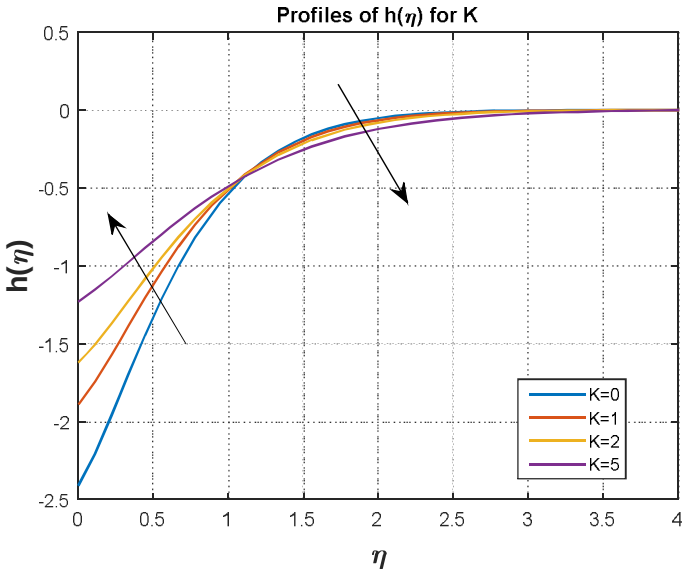

Fig. 3 Profiles of $h(\eta)$ for K

Fig. 3 shows the angular velocity profiles $h(\eta)$ for different values of the micropolar parameter K. As K increases from 0 to 5, the magnitude of the angular velocity decreases near the surface, indicating that higher micropolarity weakens the rotational motion of fluid particles. For $K = 0$, representing a non-micropolar fluid, the angular velocity has the highest initial negative peak, but this effect diminishes with increasing K, reflecting the micro-rotational resistance. All curves exhibit similar asymptotic behaviour, converging to zero as $\eta \to \infty$, ensuring the solution satisfies the boundary conditions. This behaviour emphasizes that increased micropolarity dampens particle rotation near the surface and slows the fluid's transition to equilibrium.

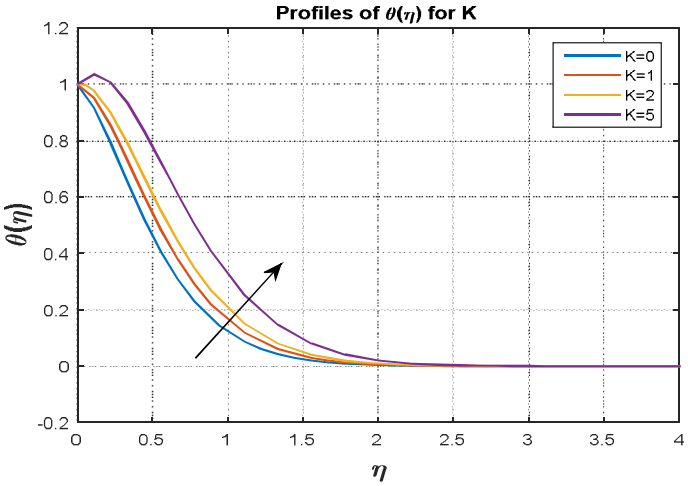

Fig. 4 Profiles of $\theta(\eta)$ for K

Fig. 4 presents the temperature profiles $\theta(\eta)$ for varying values of the micropolar parameter K. As K increases from 0 to 5, the temperature near the surface rises, reflecting the effect of micropolarity in retaining heat within the fluid. For $K = 0$, representing a Newtonian fluid, the temperature decays more rapidly along the surface, indicating more efficient thermal dissipation. As K increases, the micro-rotational effects within the fluid contribute to heat retention, resulting in a slower decay of temperature along the vertical surface.

All profiles asymptotically approach $\theta(\eta) \to 0$ as $\eta \to \infty$, satisfying the boundary condition for temperature at the free stream. This result indicates that micropolar fluids have greater thermal resistance compared to Newtonian fluids.

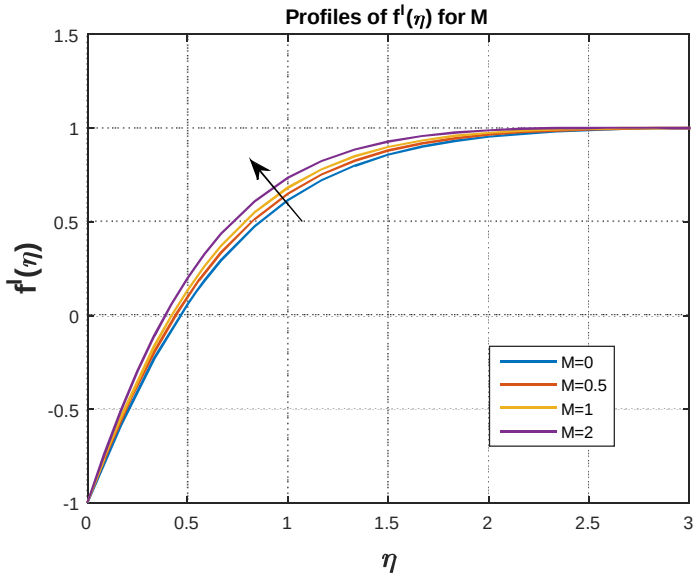

Fig. 5 Profiles of $f'(\eta)$ for M

Fig. 5 presents the velocity profiles $f'(\eta)$ for varying values of the magnetic parameter M. As M increases from 0 to 2, the velocity near the surface decreases due to the Lorentz force, which resists the fluid motion. For lower values of M, the fluid flows more freely, resulting in higher velocities along the surface. All profiles eventually converge to $\eta \to \infty$, ensuring that the boundary condition for the free-stream velocity is satisfied. This behaviour demonstrates how magnetic fields can effectively suppress fluid motion.

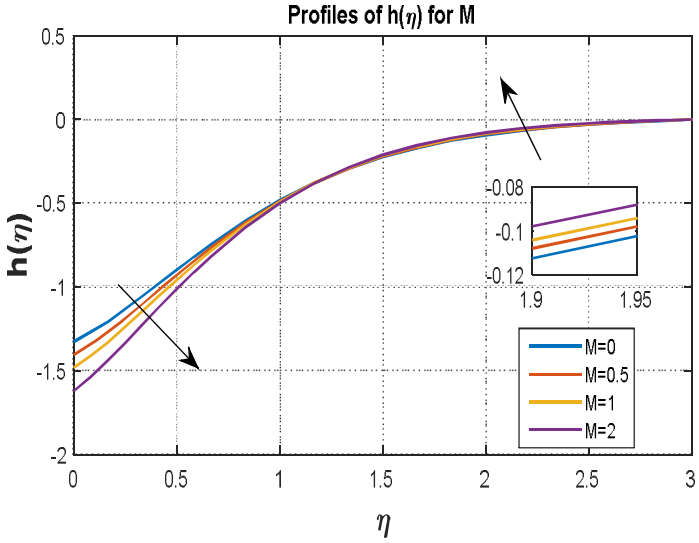

Fig. 6 Profiles of $h(\eta)$ for M

Fig. 6 displays the angular velocity profiles $h(\eta)$ for various values of the magnetic parameter M. As M increases from 0 to 2, the magnitude of the angular velocity decreases near the surface, indicating that stronger magnetic fields suppress the micro-rotational effects in the fluid. This reduction in angular velocity occurs due to the Lorentz force, which opposes fluid motion and reduces the fluid's ability to rotate internally. Despite these changes near the surface, all profiles converge toward zero as $\eta \to \infty$, confirming that the solution satisfies the boundary conditions. The inset in the figure highlights the subtle differences in the angular velocity behaviour for higher values of M, showing that the magnetic field gradually reduces micro-rotation.

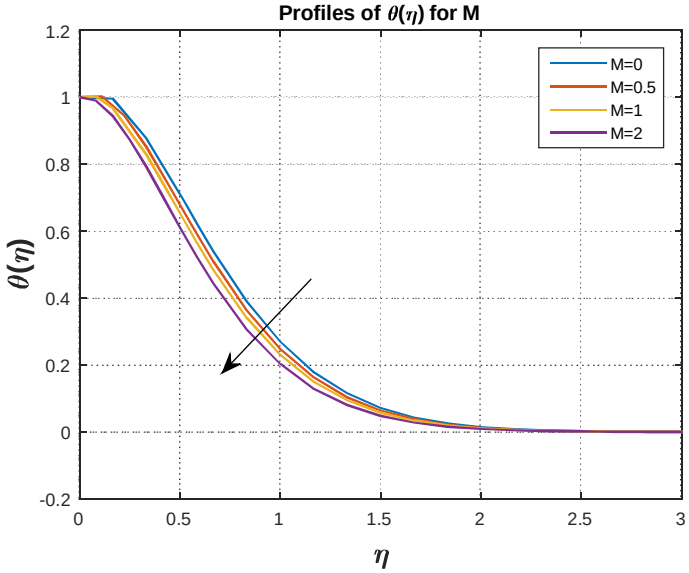

Fig. 7 Profiles of $\theta(\eta)$ for M

Fig. 7 presents the temperature profiles $\theta(\eta)$ for various values of the magnetic parameter M. As M increases from 0 to 2, the temperature near the surface decreases, indicating that the magnetic field enhances heat dissipation by suppressing fluid motion. The reduction in fluid velocity caused by the Lorentz force limits thermal conduction, leading to lower temperatures within the boundary layer.

All profiles converge asymptotically to $\theta(\eta) \to 0$ as $\eta \to \infty$, ensuring that the boundary condition for the temperature at the free stream is satisfied. The results demonstrate that higher magnetic fields promote more efficient thermal dissipation which is essential for MHD applications.

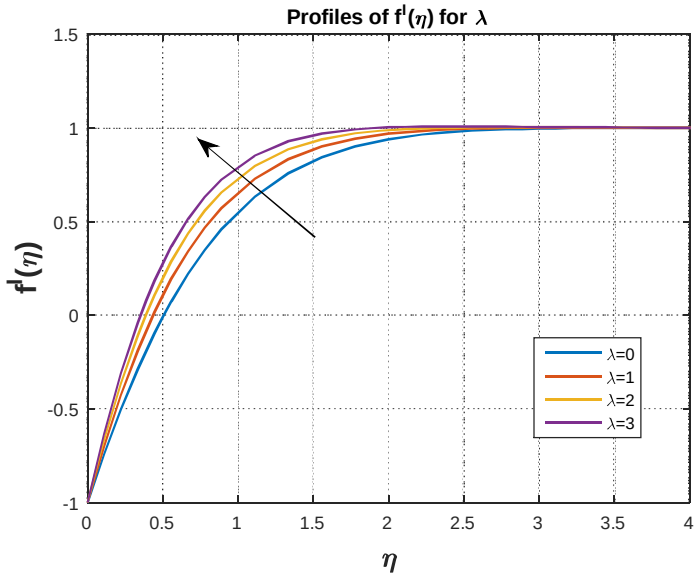

Fig. 8 Profiles of $f'(\eta)\ for\ \lambda$

Fig. 8 illustrates the velocity profiles $f'(\eta)$ for varying values of the buoyancy parameter λ. As λ increases from 0 to 3, the velocity near the surface increases. This occurs because higher buoyancy forces aid the fluid flow, reducing resistance and enhancing velocity within the boundary layer. For $\lambda = 0$, where no buoyancy effect is present, the fluid velocity is lowest, while larger values of λ result in higher velocities.

All profiles asymptotically converge to $f'(\eta) \to 1$ as $\eta \to \infty$, indicating that the free-stream velocity is achieved far from the surface. These results highlight the importance of buoyancy in enhancing fluid motion which is crucial for natural convection processes.

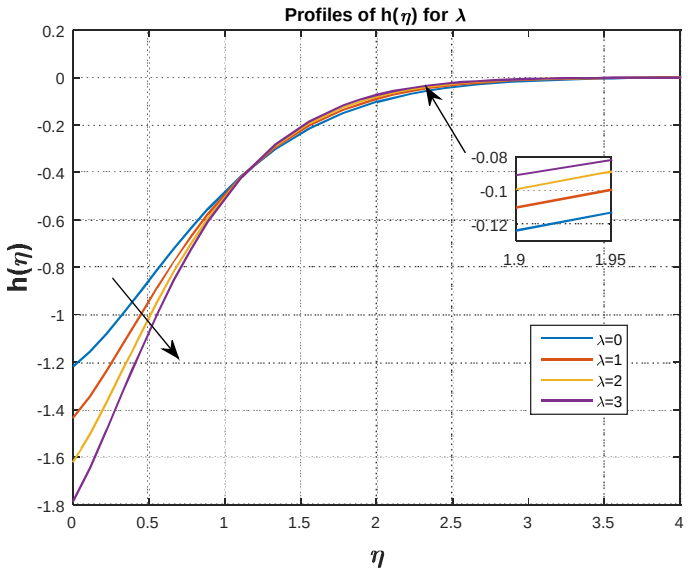

Fig. 9 Profiles of $h(\eta)$ for λ

Fig. 9 displays the angular velocity profiles $h(\eta)$ for various values of the buoyancy parameter λ. As λ increases from 0 to 3, the magnitude of the angular velocity near the surface decreases, indicating that stronger buoyancy forces reduce micro-rotational effects. This behaviour reflects how buoyancy-driven fluid motion minimizes the rotational inertia within the boundary layer, resulting in less pronounced angular velocity.

The inset in the figure highlights the subtle differences in angular velocity near the surface for higher values of λ. Despite these variations, all profiles converge toward zero as $\eta \to \infty$, satisfying the boundary conditions. These findings highlight the role of buoyancy in suppressing particle rotation.

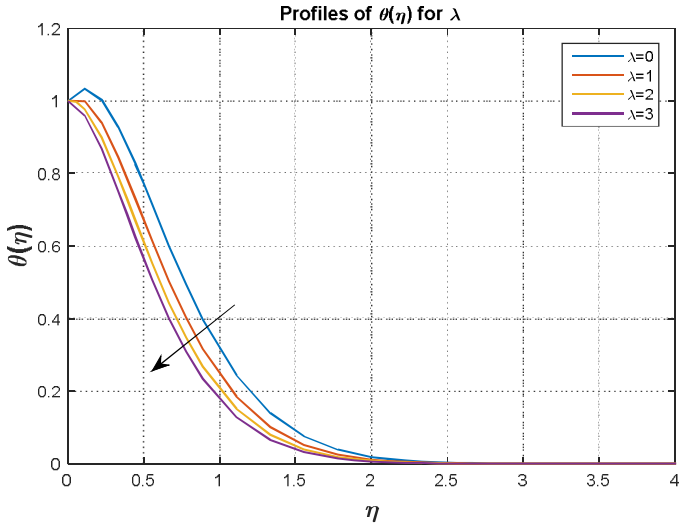

Fig. 10 Profiles of $\theta(\eta)$ for λ

Fig. 10 presents the temperature profiles $\theta(\eta)$ for varying values of the buoyancy parameter λ. As λ increases from 0 to 3, the temperature within the boundary layer decreases. This reduction indicates that higher buoyancy forces enhance the convective motion, promoting heat dissipation and lowering the temperature near the surface. For λ=0, representing the absence of buoyancy effects, the temperature remains higher, showing less effective thermal convection.

All profiles asymptotically converge to $\theta(\eta) \to 0 \; as \; \eta \to \infty$, confirming that the boundary condition for the temperature at the free stream is satisfied. These results demonstrate the role of buoyancy in improving heat transfer, which is significant for natural convection applications where buoyancy-driven flows contribute to more efficient thermal management

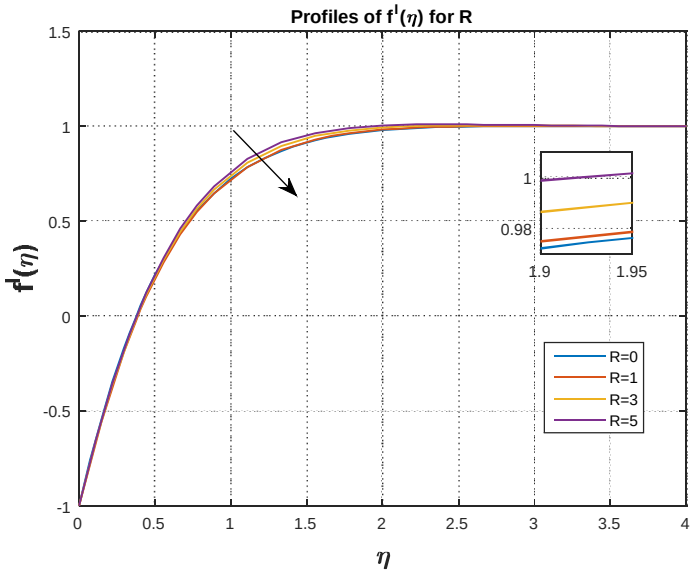

Fig. 11 Profiles of $f'(\eta)$ for R

Fig. 11 presents the velocity profiles $f'(\eta)$ for different values of the radiation parameter R. As R increases from 0 to 5, the fluid velocity near the surface slightly increases. This behaviour indicates that higher radiation enhances the thermal energy within the fluid, reducing viscosity effects and promoting fluid motion near the surface.

All profiles converge to $f'(\eta) \to 1$ as $\eta \to \infty$, ensuring that the boundary condition for the free-stream velocity is satisfied. The inset shows minor differences between the profiles for higher values of R, confirming that radiation slightly boosts velocity but does not drastically alter the flow structure. These results highlight the role of radiation in improving fluid motion, which is relevant in processes where thermal radiation affects flow behaviour, such as in high-temperature environments and thermal energy systems.

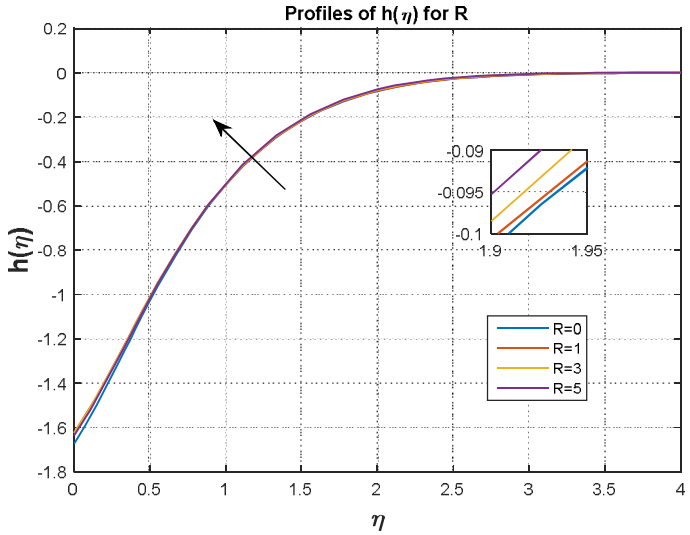

Fig. 12 Profiles of $h(\eta)$ for R

Fig. 12 shows the angular velocity profiles $h(\eta)$ for varying values of the radiation parameter R. As R increases from 0 to 5, the magnitude of the angular velocity near the surface decreases slightly. This suggests that higher radiation reduces micro-rotational effects by dissipating energy more efficiently within the boundary layer, thereby suppressing angular motion.

All profiles gradually converge to zero as $\eta \to \infty$, ensuring that the boundary conditions are satisfied. The inset highlights subtle variations in the angular velocity for different values of R, confirming that while radiation influences micro-rotation, its effect remains moderate. These findings are relevant in thermal systems where controlling micro-rotational effects is essential for stability and performance.

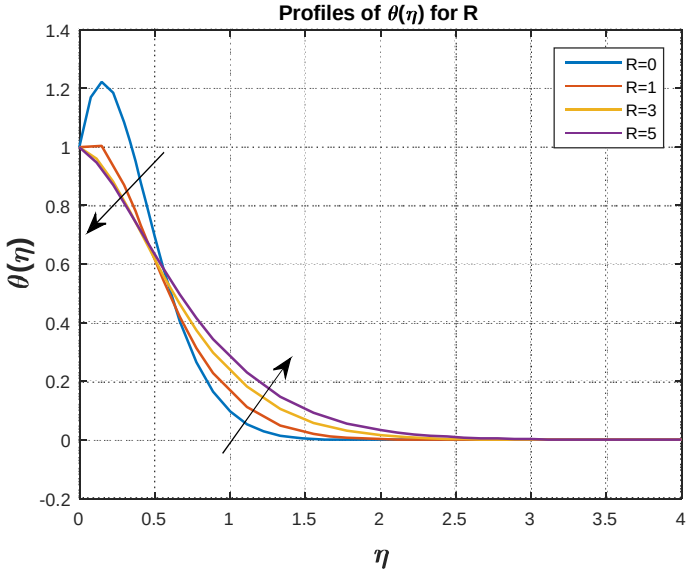

Fig. 13 Profiles of $\theta(\eta)$ for R

Fig. 13 presents the temperature profiles $\theta(\eta)$ for varying values of the radiation parameter R. As R increases from 0 to 5, the temperature near the surface decreases more rapidly, indicating that higher radiation enhances thermal energy dissipation within the boundary layer. For lower values of R, the fluid retains more heat, resulting in a slower temperature decay along the surface.
All profiles eventually converge to $\theta(\eta) \to 0$ as $\eta \to \infty$, ensuring that the boundary condition for the free-stream temperature is met. The differences between the profiles demonstrate that radiation plays a significant role in promoting heat transfer.

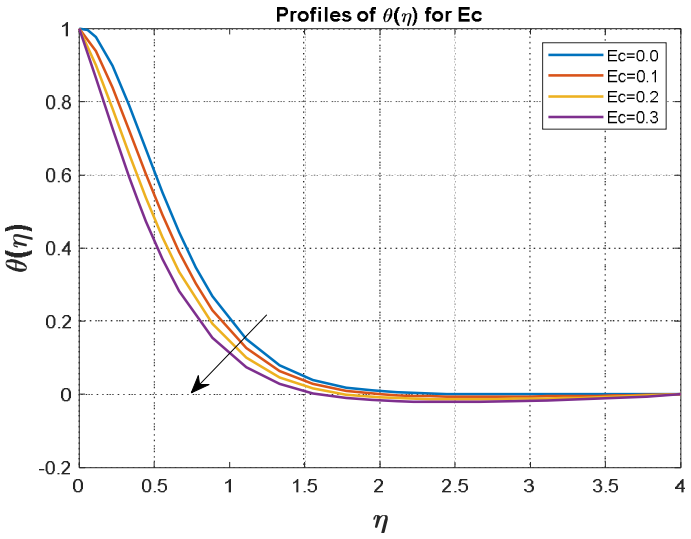

Fig. 14 Profiles of $\theta(\eta)$ for Ec

Fig. 14 displays the temperature profiles $\theta(\eta)$ for varying values of the Eckert number Ec, which reflects the impact of viscous dissipation on heat generation. As Ec increases from 0 to 0.3, the temperature within the boundary layer increases, indicating that higher viscous dissipation generates more heat, thereby raising the fluid temperature. The profile for Ec=0 represents the case with no dissipation, showing the lowest temperature.

All profiles eventually converge to $\theta(\eta) \to 0$ as $\eta \to \infty$, ensuring that the boundary condition at the free stream is satisfied. These results demonstrate the importance of viscous dissipation in systems where mechanical energy converts into heat such as in lubrication and high-speed flows.

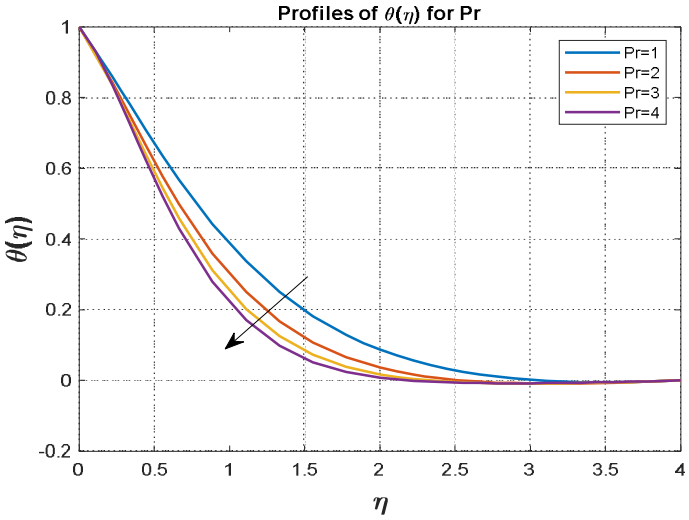

Fig. 15 Profiles of $\theta(\eta)$ $for\ Pr$

Fig. 15 presents the temperature profiles θ(η) for varying values of the Prandtl number Pr. As Pr increases from 1 to 4, the temperature within the boundary layer decreases more rapidly, indicating that fluids with higher Prandtl numbers dissipate heat more efficiently. This is because higher Pr values correspond to fluids with lower thermal diffusivity, causing faster cooling near the surface.

All profiles converge to θ(η)→0 as η→∞, confirming that the boundary condition for the free-stream temperature is satisfied. These findings demonstrate that fluids with higher Prandtl numbers, such as oils, cool faster than those with lower Prandtl numbers such as gases.

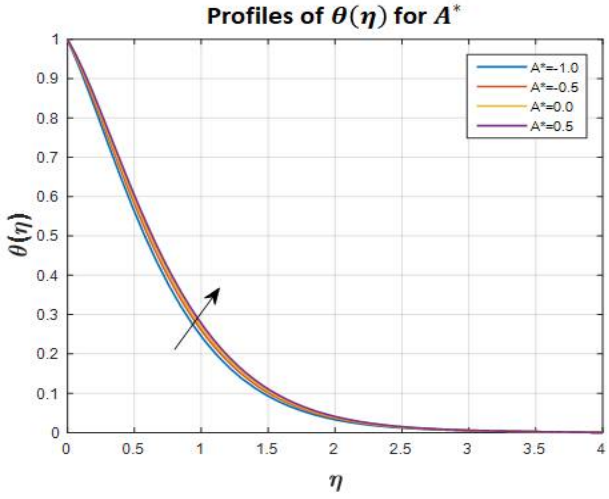

Fig. 16 Profiles of $\theta(\eta)$ for A^*

Fig. 16 illustrates the variation of the dimensionless temperature profile $\theta(\eta)$ with the similarity variable η for different values of the heat source/sink parameter A^*. It is observed that as A^* increases from -1.0 to 0.5, the temperature distribution $\theta(\eta)$ increases throughout the boundary layer. This behaviour signifies that the presence of a heat source enhances thermal energy within the flow, resulting in higher fluid temperatures. Conversely, for negative values of A^*, which correspond to a heat sink, the temperature decays more rapidly, indicating a cooling effect.

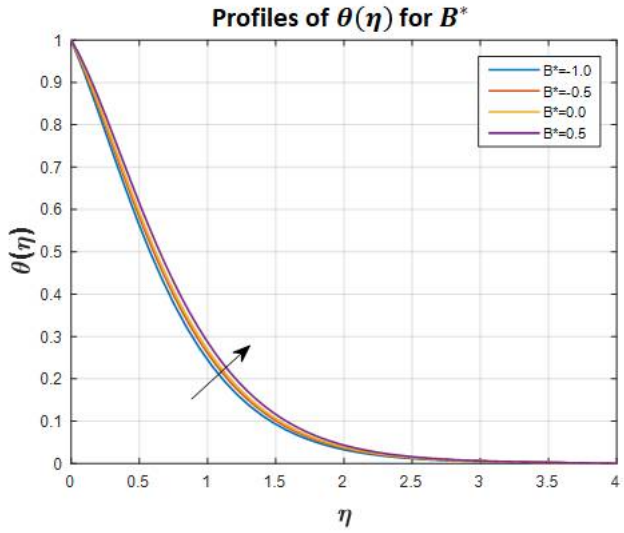

Fig. 17 Profiles of $\theta(\eta)$ for B^*

Fig. 17 presents the influence of the non-uniform heat source/sink parameter B^* on the dimensionless temperature distribution $\theta(\eta)$. An increase in B^* from -1.0 to 0.5 leads to a corresponding rise in the temperature profile. Similar to the behaviour of A^*, a positive value of B^* implies the existence of additional internal heat generation, which elevates the thermal boundary layer temperature. In contrast, a negative B^* intensifies heat removal, leading to a steeper temperature gradient and reduced fluid temperature.

V. CONCLUSION

This investigation focuses on the thermal study and magnetohydrodynamic (MHD) micropolar fluid of stagnation-point flow across a vertically aligned surface undergoing exponential stretching or shrinking, incorporating the effects of buoyancy. The analysis confirmed the existence of solutions under both stretching and shrinking scenarios. The study further elaborates on the influence of magnetic forces, buoyancy-induced flow, thermal radiation, energy dissipation due to viscosity, and the rotational characteristics of micropolar fluids over the exponentially varying surface. From this comprehensive analysis, the study has led to the derivation of several important findings.

1) The velocity declines with increasing micropolar effects due to rotational inertia, the magnetic fields suppress the velocity through Lorentz forces, but increase under the consequence of magnetic fields, radiation and buoyancy forces enhancing the fluid's motion.
2) The angular velocity decreases with both buoyancy forces and magnetic fields, showing that these parameters suppress micro-rotational effects within the fluid.
3) The temperature drops with growing magnetic fields and buoyancy forces due to enhanced convective heat transfer but increases with higher micropolar effects, which retain heat. Radiation enhances heat dissipation, lowering the temperature near the surface.
4) Higher Prandtl numbers accelerate heat dissipation, resultant in a supplementary rapid decline in temperature within boundary layer, while higher Eckert numbers increase the temperature due to viscous dissipation.
5) As the fluid temperature rises because of increased viscous dissipation, the thermal boundary layer next to the surface expands.
6) Buoyancy forces promote velocity and improve heat transfer by enhancing fluid motion by providing additional control over the flow.
7) Radiation and micropolar parameters influence both energy transfer and rotational behaviour, with radiation enhancing heat transfer and micropolarity slowing down fluid motion and retaining heat.
8) It is evident from the findings that higher values of the heat source/sink parameters A^* and B^* contribute to an increase in the thermal energy of the fluid. In contrast, negative values enhance the rate of temperature reduction. Therefore, these parameters are crucial in regulating the thermal behaviour across the boundary layer.

REFERENCES

[1] Sakiadis, B. C. (1961). Boundary-layer behaviour on continuous solid surfaces: I. Boundary-layer equations for two-dimensional and axisymmetric flow. AIChE Journal, 7(1), 26-28.
[2] Sikiadis, B. C. (1961). Boundary-Layer behaviour on continuous solid surfaces. AI Ch. EJ, 7, 26-28.
[3] Crane, L. J. (1970). Flow past a stretching plate. Zeitschrift für angewandte Mathematik und Physik ZAMP, 21, 645-647.
[4] Gupta, P. S., & Gupta, A. S. (1977). Heat and mass transfer on a stretching sheet with suction or blowing. The Canadian journal of chemical engineering, 55(6), 744-746.
[5] Sandeep, N., & Sulochana, C. (2015). Dual solutions for unsteady mixed convection flow of MHD micropolar fluid over a stretching/shrinking sheet with non-uniform heat source/sink. Engineering Science and Technology, an International Journal, 18(4), 738-745.
[6] Prasannakumara, B. C., Gireesha, B. J., & Manjunatha, P. T. (2015). Melting phenomenon in MHD stagnation point flow of dusty fluid over a stretching sheet in the presence of thermal radiation and non-uniform heat source/sink. International Journal for Computational Methods in Engineering Science and Mechanics, 16(5), 265-274.
[7] Mabood, F., Ibrahim, S. M., Rashidi, M. M., Shadloo, M. S., & Lorenzini, G. (2016). Non-uniform heat source/sink and Soret effects on MHD non-Darcian convective flow past a stretching sheet in a micropolar fluid with radiation. International Journal of Heat and Mass Transfer, 93, 674-682.
[8] Seth, G. S., Sharma, R., Kumbhakar, B., & Tripathi, R. (2017). MHD stagnation point flow over exponentially stretching sheet with exponentially moving free-stream, viscous dissipation, thermal radiation and non-uniform heat source/sink. In Diffusion Foundations (Vol. 11, pp. 182-190). Trans Tech Publications Ltd.
[9] Ram, M. S., Shamshuddin, M. D., & Spandana, K. (2021). Numerical simulation of stagnation point flow in magneto micropolar fluid over a stretchable surface under influence of activation energy and bilateral reaction. International Communications in Heat and Mass Transfer, 129, 105679.
[10] Murugan, R. D., Sivakumar, N., Tarakaramu, N., Sarhan, N., & Awwad, E. M. (2024). Mixed convection hybrid nanofluid flow over a rotating cone in a rotating fluid environment with interfacial nanolayer effect. Numerical Heat Transfer, Part B: Fundamentals, 1-20.
[11] Murugan, R. D., Sivakumar, N., Tarakaramu, N., Ahmad, H., & Askar, S. (2024). Entropy generation on MHD motion of hybrid nanofluid with porous medium in presence of thermo-radiation and ohmic viscous dissipation. Discover Applied Sciences, 6(4), 199.
[12] Murugan, R. D., Sivakumar, N., Tarakaramu, N., Alhazmi, H., & Abdullaev, S. (2024). Entropy and energy transfer analysis of a Maxwell thin-film fluid over an inclined surface with viscous dissipation effect. ZAMM-Journal of Applied Mathematics and Mechanics/Zeitschrift für Angewandte Mathematik und Mechanik, e202300381.
[13] Tarakaramu, N., Sivakumar, N., Tamam, N., Satya Narayana, P. V., & Ramalingam, S. (2024). Theoretical analysis of Arrhenius activation energy on 3D MHD nanofluid flow with convective boundary condition. Modern Physics Letters B, 38(16), 2341009.
[14] Tarakaramu, N., Reddappa, B., Radha, G., Abduvalieva, D., Sivakumar, N., Awwad, F. A., ... & Reddy, K. A. (2023). Thermal radiation and heat generation on three-dimensional Casson fluid motion via porous stretching surface with variable thermal conductivity. Open Physics, 21(1), 20230137.
[15] Masthanaiah, Y., Tarakaramu, N., Khan, M. I., Rushikesava, A., Moussa, S. B., Fadhl, B. M., ... & Eldin, S. M. (2023). Impact of viscous dissipation and entropy generation on cold liquid via channel with porous medium by analytical analysis. Case Studies in Thermal Engineering, 47, 103059.
[16] Jagadeesh, S., Chenna Krishna Reddy, M., Tarakaramu, N., Ahmad, H., Askar, S., & Shukhratovich Abdullaev, S. (2023). Convective heat and mass transfer rate on 3D Williamson nanofluid flow via linear stretching sheet with thermal radiation and heat absorption. Scientific Reports, 13(1), 9889.
[17] Reddy, A. B., & Kumar, R. Y. R. (2022, December). Performance and security analysis in cloud using drops and T-coloring methods. In 2022 Fourth International Conference on Emerging Research in Electronics, Computer Science and Technology (ICERECT) (pp. 1-7). IEEE.
[18] Li, S., Tarakaramu, N., Khan, M. I., Sivakumar, N., Satya Narayana, P. V., Abdullaev, S., ... & Eldin, S. M. (2024). Enhanced heat transfer and fluid motion in 3D nanofluid with anisotropic slip and magnetic field. Open Physics, 22(1), 20230131.
[19] Sedki, A. M., & Qahiti, R. (2023). Unsteady magnetohydrodynamic radiative Casson nanofluid within chemically reactive flow over a stretchable surface with variable thickness through a porous medium. Energies, 16(23), 7776.
[20] Rehman, Fiaz Ur, Sohail Nadeem, Hafeez Ur Rehman, and Rizwan Ul Haq. "Thermophysical analysis for three-dimensional MHD stagnation-point flow of nano-material influenced by an exponential stretching surface." Results in physics 8 (2018): 316-323. https://doi.org/10.1016/j.rinp.2017.12.026
[21] Bejawada, S. G., & Nandeppanavar, M. M. (2023). Effect of thermal radiation on magnetohydrodynamics heat transfer micropolar fluid flow over a vertical moving porous plate. Experimental and Computational Multiphase Flow, 5(2), 149-158.
[22] Bakar, F. N. A., & Soid, S. K. (2023). MHD Stagnation-Point Flow and Heat Transfer in a Micropolar Fluid over an Exponentially Vertical Sheet. CFD Letters, 15(3), 81-96.
[23] Khan, M. N., Ahmad, S., Wang, Z., Ahammad, N. A., & Elkotb, M. A. (2023). Bioconvective surface-catalyzed Casson hybrid nanofluid flow analysis by using thermodynamics heat transfer law on a vertical cone. Tribology International, 188, 108859.
[24] Khan, M. N., Aldosari, F. M., Wang, Z., Yasir, M., Afikuzzaman, M., & Elseesy, I. E. (2024). Overview of solar thermal applications of heat exchangers with thermophysical features of hybrid nanomaterials. Nanoscale Advances, 6(1), 136-145.
[25] Khan, M. N., Ahmad, S., Wang, Z., Hussien, M., Alhuthali, A. M., & Ghazwani, H. A. (2024). Flow and heat transfer insights into a chemically reactive micropolar Williamson ternary hybrid nanofluid with cross-diffusion theory. Nanotechnology Reviews, 13(1), 20240081.
[26] Khan, M. N., Wang, Z., Ahammad, N. A., Rezapour, S., Shutaywi, M., Ali, N. B., & Elkotb, M. A. (2024). Mixed convective flow analysis of a Maxwell fluid with double diffusion theory on a vertically exponentially stretching surface. Applied Water Science, 14(8), 172.
[27] Naveed Khan, M., Alhowaity, A., Wang, Z., Gepreel, K. A., & Hussien, M. (2024). Numerical analysis of the heat transfer application on a convective tangent hyperbolic nanofluid flow over a porous stretching cylinder with stratification effects. Numerical Heat Transfer, Part A: Applications, 1-17.
[28] Waini, Iskandar, Anuar Ishak, and Ioan Pop. "Hybrid nanofluid flow towards a stagnation point on an exponentially stretching/shrinking vertical sheet with buoyancy effects." International Journal of Numerical Methods for Heat & Fluid Flow 31, no. 1 (2020): 216-235.
[29] Bakar, F. N. A., & Soid, S. K. (2023). MHD Stagnation-Point Flow and Heat Transfer in a Micropolar Fluid over an Exponentially Vertical Sheet. CFD Letters, 15(3), 81-96.
[30] Yasir, M., Khan, M., & Malik, Z. U. (2023). Analysis of thermophoretic particle deposition with Soret-Dufour in a flow of fluid exhibit relaxation/retardation times effect. International Communications in Heat and Mass Transfer, 141, 106577.

[31] Khan, M. N., Haider, J. A., Wang, Z., Gul, S., Lone, S. A., & Elkotb, M. A. (2024). Mathematical modelling of the partial differential equations in microelectromechanical systems (MEMS) and its applications. Modern Physics Letters B, 38(05), 2350207.

[32] Yasir, M., Bilal, S., Ahammad, N. A., & Elseesy, I. E. (2024). Thermal irregular generation and absorption of nanoscale energy transportation of thermodynamic material of a micropolar fluid. Ain Shams Engineering Journal, 15(9), 102948.

[33] Yasir, M., Khan, M., Al-Zubaidi, A., & Saleem, S. (2023). Arrhenius activation energy effect in thermally viscous dissipative flow of micropolar material with gyrotactic microorganisms. Alexandria Engineering Journal, 84, 204-214.

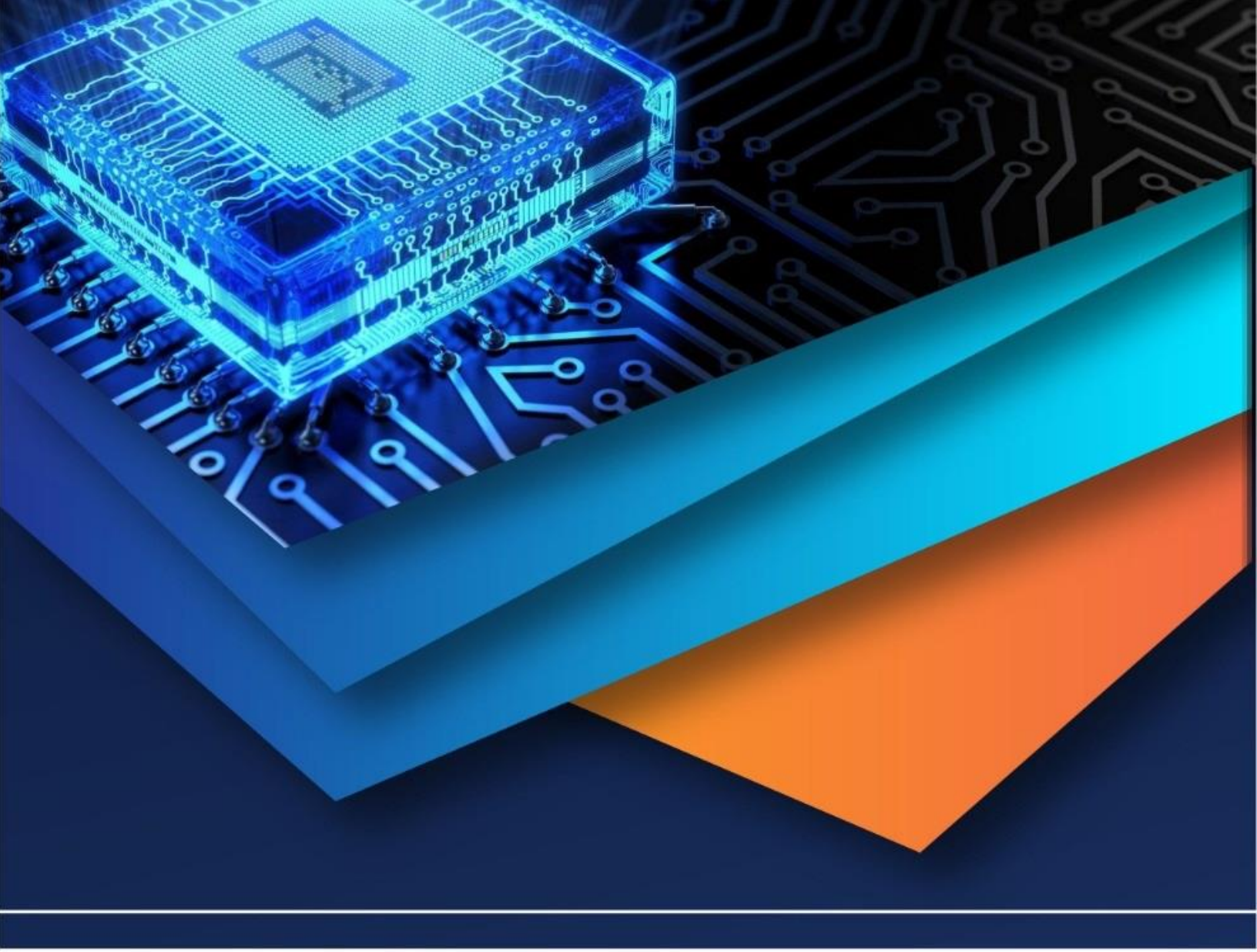

10.22214/IJRASET

45.98

IMPACT FACTOR: 7.129

IMPACT FACTOR: 7.429

INTERNATIONAL JOURNAL FOR RESEARCH

IN APPLIED SCIENCE & ENGINEERING TECHNOLOGY